

SolarPACES 2013

A high-temperature, high-efficiency solar thermoelectric generator prototype

M. L. Olsen^a, E. L. Warren^b, P. A. Parilla^a, E. S. Toberer^{a,b}, C. E. Kennedy^a, G. J. Snyder^c, S. A. Firdosy^d, B. Nesmith^d, A. Zakutayev^a, A. Goodrich^a, C. S. Turchi^a, J. Netter^a, M. H. Gray^a, P. F. Ndione^a, R. Tirawat^a, L. L. Baranowski^b, A. Gray^a, and D. S. Ginley^a

^aNational Renewable Energy Laboratory (NREL), Golden, CO 80401, USA

^bColorado School of Mines, Golden, CO 80401, USA

^cCalifornia Institute of Technology, Pasadena, CA 91125, USA

^dJet Propulsion Laboratory (JPL), California Institute of Technology, Pasadena, CA 91109, USA

Abstract

Solar thermoelectric generators (STEGs) have the potential to convert solar energy at greater than 15% efficiency. This project investigates the system design, the necessary thermoelectric and optical technologies, and the economic feasibility of the STEG approach. A STEG is a solid-state heat engine that converts sunlight directly into DC electricity through the thermoelectric effect. STEGs consist of three subsystems: the solar absorber, the thermoelectric generator (TEG), and the heat management system (insulation, heat exchanger, vacuum enclosure, etc.). This project will integrate several state-of-the-art technologies to achieve high efficiency, including next-generation materials for TEGs, high-temperature solar-selective absorbers, and thermal cavities. We will test STEGs at NREL's high flux solar furnace (HFSF) and perform analysis of parasitic losses and lifetime analysis to optimize prototype operation. Equally important for this technology is the development of a cost model to determine the economic competitiveness and possible application niches for STEG technologies. We report on first-order economic analysis to identify the most promising pathways for advancing the technology.

© 2013 The Authors. Published by Elsevier Ltd. This is an open access article under the CC BY-NC-ND license (<http://creativecommons.org/licenses/by-nc-nd/3.0/>).

Selection and peer review by the scientific conference committee of SolarPACES 2013 under responsibility of PSE AG.

Final manuscript published as received without editorial corrections.

Keywords: solar thermoelectric generators; solar-selective absorbers; solar cavity-receivers; solid-state heat engines

1. Introduction

Solar thermoelectric generators (STEGs), like photovoltaic systems and concentrating solar power plants, generate electricity by harnessing the energy of sunlight. Because STEGs are solid-state devices, their lack of moving parts or need for high-temperature operating fluids and their robustness in harsh environments make them an attractive technology for standalone power conversion or in hybrid solar-thermal systems. While the traditionally low efficiency of thermoelectric devices has relegated their use to such applications as waste heat recovery [1, 2], recent improvements in thermoelectric devices [3] may make STEGs a viable technology for direct solar-to-electric energy conversion.

STEGs operate by absorbing sunlight, which generates a temperature gradient, which in turn, generates electricity through the Seebeck effect. The efficiency of a STEG, therefore, depends on both the efficiency with which sunlight is converted to heat and on the thermoelectric efficiency of the device. The thermoelectric efficiency depends on the temperature difference across the device and the temperature-dependent figure of merit of the thermoelectric materials, $zT = (S^2\sigma/k)T$, where S is the Seebeck coefficient, σ is the electrical conductivity, k is the thermal conductivity, and T is the absolute temperature. The maximum efficiency [4] of a TEG is given by

$$\eta_{TE} = \left(1 - \frac{T_C}{T_H}\right) \frac{\sqrt{1 + Z\bar{T}} - 1}{\sqrt{1 + Z\bar{T}} + \frac{T_C}{T_H}} \quad (1)$$

Here, the term in parentheses is the Carnot efficiency, where T_H is the temperature of the hot side of the device, T_C is the cold-side temperature, Z is the effective figure of merit across the temperature gradient, and $\bar{T} = (T_H + T_C)/2$.

The total efficiency of the STEG is the product of η_{TE} and the absorber efficiency η_{abs} [5], which depends not only on the amount of sunlight that is absorbed but also on the amount of heat lost from the surface. Historically, STEGs have suffered from low efficiencies. The reasons for this come from two sources: low Carnot efficiency due to a relatively small temperature drop across the devices and losses inherent to the thermoelectric materials. The first reported STEG with an appreciable efficiency (3.35%) was composed of p-type ZnSb alloys and n-type Bi+Sb alloys and was operated with a temperature difference, $\Delta T = T_H - T_C = 247$ °C [6]. Improving the efficiency of such devices requires increasing temperature differences and improving materials. There are two main approaches to increasing the temperature difference in a STEG: (i) optical concentration of sunlight to increase the heat flux at the absorber surface, and (ii) thermal concentration, in which the area of a highly thermally conducting absorber is greater than the area of the thermoelectric legs, allowing for increased heat flux through the legs. The latter approach was recently employed to demonstrate STEG devices with efficiencies of 4.6% and 5.2% with light intensities corresponding to 1 kW/m² (AM1.5G) and 1.5 kW/m², respectively [7]. The STEGs studied were composed of nanostructured Bi₂Te₃-based alloys with an effective $ZT = 1.03$ at the optimum operating temperature (100 °C) [8, 9].

In recent years, work with nanostructured and complex bulk materials has led to significant improvement in thermoelectric materials with many materials exhibiting ZT in excess of unity over a broad range of temperatures [10–14]. In 2011, several of these next-generation materials were combined to achieve the highest-efficiency TEG ever reported: 15% efficiency across $T_H - T_C = 1000$ –200 °C [3]. This device consisted of a segmented n-type leg composed of skutterudite and La₃Te₄ and p-type leg of skutterudite and Yb₁₄MnSb₁₁.

In this work, our team is developing a STEG prototype that employs the state-of-the-art TEG mentioned above with high optical concentration (200–300 Suns at the absorber surface to achieve a sunlight-generated $T_H = 1000$ °C) with a targeted total efficiency of 15%. In addition to the efficient TEG, to reach the efficiency target, the prototype STEG requires (i) an absorber that is well matched to the solar spectrum, (ii) minimal heat losses due to thermal radiation, (iii) a vacuum environment to eliminate convective heat losses and prevent degradation of the STEG, and (iv) an additional, actively cooled Bi₂Te₃ thermoelectric stage, which is expected to increase the total TEG efficiency to 18% by allowing for a lower T_C . To simultaneously meet requirements (i) and (ii), we are developing a solar-selective absorber, which will be coupled with a thermally insulating cavity. The prototype design is shown in Fig. 1.

Additionally, we are developing a cost model to assess the economic competitiveness of STEGs both as a standalone energy-conversion technology and as a topping cycle for existing concentrating solar power (CSP) technologies. Initial analysis identifies both a stand-alone dish-based system and hybrid STEG-CSP systems as promising avenues for this technology.

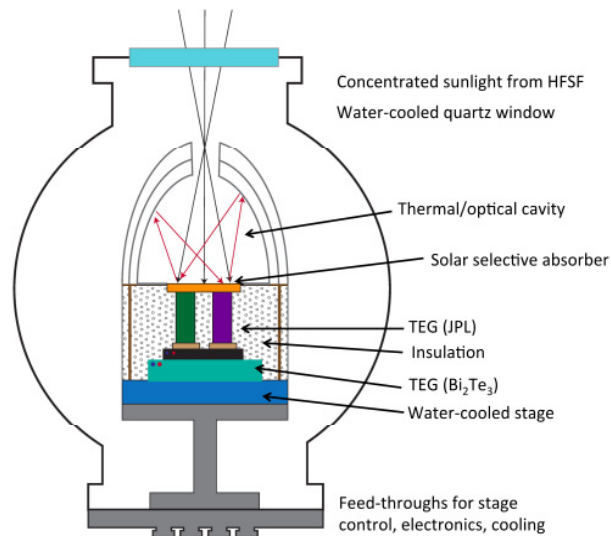


Fig. 1. Schematic of the STEG prototype.

Nomenclature

ZT	effective thermoelectric figure of merit
T_H	hot-side temperature
T_C	cold-side temperature
ΔT	operating temperature range ($T_H - T_C$)
η_{TE}	thermoelectric efficiency
η_{TE}	absorber efficiency

2. STEG prototype components

To produce a high-efficiency STEG, several state-of-the-art technologies must be integrated. As discussed above, a module formed from several of the high-efficiency TEG couples developed at JPL will serve as the power-generating device. Maximizing the solar absorptance while minimizing losses due to blackbody radiation at the hot side will be critical to maintaining high efficiency under solar illumination. Thus, the project includes an effort to incorporate an improved solar-selective absorber coating that will allow for high absorptance over the solar spectrum while inhibiting emittance of the blackbody spectrum at 1000 °C. The STEG prototype design shown in Fig. 1 also includes a thermally insulating cavity that will allow concentrated sunlight to enter through an aperture but further limit radiative losses. Concentrated sunlight will be provided by NREL's high-flux solar furnace with the addition of secondary optics to tailor the geometry of the beam to the prototype.

2.1. Solar-selective absorber

Efficient conversion of sunlight to heat requires an absorber surface with high absorptivity over the solar spectrum. However, by Kirchoff's Law, this also invokes a high emissivity, leading to large radiative losses. This conflict can be resolved with a solar-selective absorber. An ideal solar-selective absorber has unity absorptance in the short-wavelength range of the solar spectrum with a step transition to zero absorptance in the infrared region to prevent emittance of blackbody radiation. The transition occurs at a cutoff wavelength that depends both on the temperature of the absorber surface and the optical concentration. NREL has a concerted effort toward improving and developing selective absorber technology. NREL researchers have patented a multilayer solar-selective coating based on inherently high-temperature oxidation-resistant TiSi materials intended for operation at 500 °C [15]. The deposited 9-layer coating achieved a measured absorptance of 0.937 and emittance of 0.24 at room temperature and 0.34 at 500 °C.

The 1000 °C operating temperature of the STEG requires modification of the multilayer coating to optimize performance at the elevated temperature. Optimization includes changes in layer thicknesses and a lower targeted cutoff wavelength. Figure 2a shows the modeled spectral performance for a 9-layer stack optimized for 1000 °C. The predicted performance of this design is better than any commercially available product, with average absorption of 0.976 over the band from 300-1300 nm and total solar-weighted absorptance of 0.938. The calculated emittance of the design is 0.21. Figure 2b shows the measured room-temperature spectral reflectance for a 9-layer stack as deposited and after high-temperature annealing. After annealing at 1000 °C, the film retains a high room-temperature absorptance of 0.884. However, the infrared reflectance is lower than predicted. We are currently measuring the optical properties of annealed individual layers to use as inputs in the model (rather than literature values) for improved as-deposited performance. We are also exploring different deposition conditions to produce films with better purity of the targeted crystalline phases for the individual layers and examining alternate material systems to improve the selectivity of the deposited films.

2.2. Thermally insulating cavity

As shown in Fig. 1, the STEG prototype design also includes a cavity to physically block thermal radiation from escaping and redirect it to the absorber surface. The operating principle of the cavity is that concentrated sunlight is focused to a waist and enters through a small aperture at the top of the cavity. The light diverges inside the cavity to fully irradiate the absorber surface. Any sunlight that is reflected by the absorber or blackbody radiation that is emitted from the surface is then (i) reflected by the cavity, (ii) absorbed and thermally reemitted by the cavity, or (iii) lost through the aperture. The proper choice of cavity geometry can increase the probability that the reflected light will be directed back toward the absorber surface. Using multiple layers of foil for the cavity improves its insulating behavior, increasing the probability that thermal radiation will be reemitted into the cavity and absorbed by the device rather than lost through the walls [16]. Designing the cavity such that the area of the aperture is much smaller than the absorber area limits the solid angle through which radiation can escape.

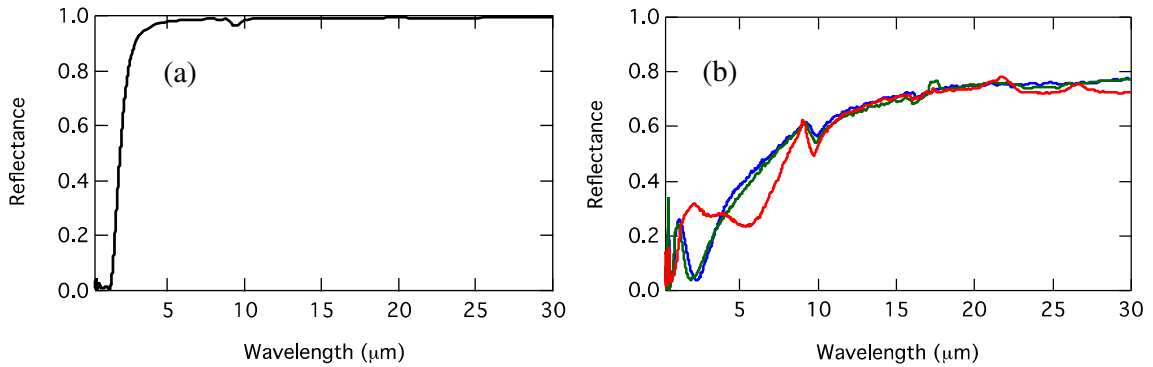


Fig. 2. (a) Spectral reflectance results from initial modeling of a 1000 °C coating. (b) Measured room-temperature spectral reflectance of a 9-layer coating as deposited (blue curve) and after annealing at 730 °C (green curve) and 1000 °C (red curve).

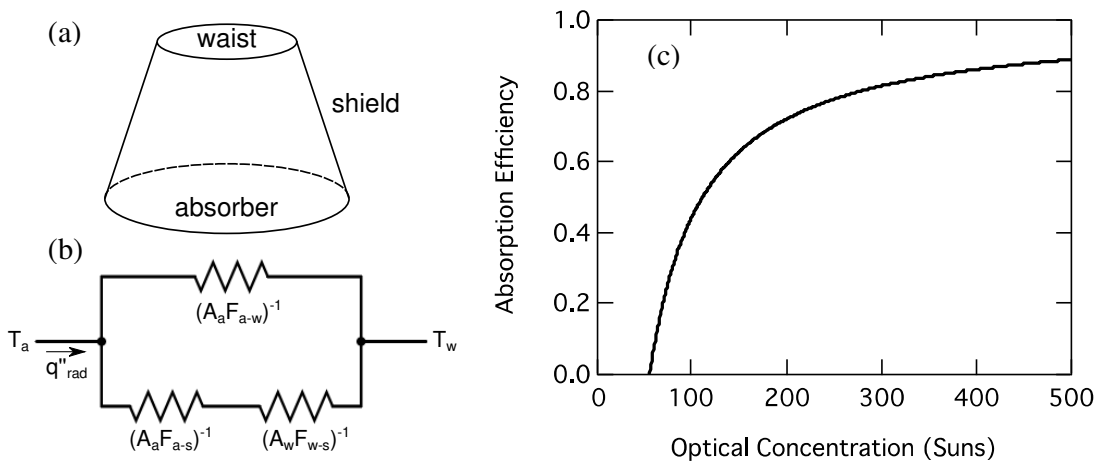


Fig. 3. Thermal/optical cavity modeling approach. (a) Solar radiation is focused to a waist where it enters the cavity and heats the absorber surface. The shield serves to limit the solid angle over which radiative losses can occur. (b) The physical model can be translated to a thermal circuit model where T_w and T_a are the temperatures of the blackbody emitters at the waist and absorber surface, respectively. The resistances to heat loss (q''_{rad}) in the system depend on the surface areas of the components (A_i) and the geometric view factors (F_{i-j}). (c) The absorption efficiency for $T_H = 1000$ °C, calculated for a cavity with $A_a/A_w = 2$, is shown as a function of the optical concentration at the absorber.

We are using a thermal circuit model to optimize the geometry of the cavity. Figure 3a shows a simplified single-layer, perfectly insulating cavity in the form of a truncated cone. The absorber is assumed to have unity absorption across all wavelengths. Both the aperture and absorber are modeled as blackbody emitters at different temperatures, while the inner surface of the shield is assumed to be opaque, diffuse, and at constant temperature. The physical model of the cavity is translated to a thermal circuit as shown in Fig. 3b with the cavity creating resistance to heat loss from the absorber, which depends on the surface area and view factor of each component [17]. Figure 3c shows the calculated absorber efficiency as a function of the optical concentration at the absorber surface for a cavity where the ratio of the absorber area to aperture area, $A_a/A_w = 2$. Achieving the 15% efficiency goal requires an absorber efficiency of 85% (i.e. $\eta_{TE} \eta_{abs} = 0.18 \times 0.85 = 0.15$), which can be reached with concentration at the absorber <300 Suns. Through this thermal model, we are optimizing the physical parameters of the cavity including shape, number of insulating layers, and the ratio of the aperture radius to the absorber radius, which defines the required convergence angle of the incoming sunlight.

2.3. Optical concentration

To reach the targeted hot-side temperature of 1000 °C, we will employ optical concentration of the incoming sunlight. As discussed above, with sufficient suppression of heat losses, through the use of a selective absorber, cavity, and vacuum enclosure, an optical concentration at the absorber surface <300 Suns should be sufficient. However, as depicted in Figs. 1 and 3a, the use of the thermally insulating cavity requires that the sunlight be focused to a waist to enter the cavity and then diverge to completely irradiate the absorber surface. Therefore, the maximum optical concentration in the system, which occurs at the focus, will be determined by the size of the cavity's aperture and the divergence of the beam.

3. High-flux solar furnace (HFSF)

We will test STEGs with NREL's HFSF, which consists of a 32-m² mirrored tracking heliostat and 25 hexagonal curved mirrors that concentrate solar radiation, providing flux up to 2,500 Suns. The array of 25 hexagonal mirrors, or primary concentrator, delivers a beam with a $e^{-1/2}$ radius of 3 cm at the focus with a convergence angle of 15°. To reduce the concentration to the targeted 200 – 300 Suns on the absorber, we will use only a subset of the array by covering the complementary mirrors. The optical concentration can be further controlled through the use of a set of specially designed blinds that also improve the spatial uniformity of the beam at the focus.

The prototype TEG module will have hot-side dimensions of ~2 cm × 2 cm, which is smaller than the beam waist delivered by the primary concentrator. As discussed above, the thermal cavity requires that the beam enter through an aperture that is smaller than the absorber and diverge to completely irradiate the absorber surface. Therefore, to capitalize on the improved absorber efficiency afforded by the thermal cavity, we must add secondary optics to tailor the incoming beam to the STEG prototype.

To optimize the delivery of flux to the STEG, we have modeled the HFSF and secondary optics using SolTrace, a software tool developed at NREL to model concentrating solar power systems [18]. This ray-tracing package enables a robust description of the solar flux delivered by the combined optical system (heliostat, primary concentrator, and secondary optics) using a realistic sun shape and optical surface parameters. Figure 4 shows the size of the focusing beam as a function of position along the beam axis. We have performed 2-D Gaussian fits to the intensity profiles calculated using SolTrace. In the vicinity of the focus (± 30 cm), the intensity profile is well described by a Gaussian, while far from the focus, the individual mirrors of the primary concentrator are imaged (Fig. 4d). We have verified the model by measuring the beam size near the focus for the 1- and 3-mirror subarrays. Figure 4b shows good agreement between the model and the beam size measured by placing a target in the beam path and imaging with an infrared camera.

To accommodate the small size of the STEG and aperture in the cavity, we will place secondary focusing optics in the beam path to further tighten the beam waist. We have modeled a series of lenses with different numbers of primary mirrors to identify the optimum optical components for integrating the STEG prototype into the HFSF. The key parameters for selection are: (i) the area of the beam at the waist, which defines the aperture in the cavity, (ii) the distance from the focus at which the beam completely fills the absorber area, which defines the height of the cavity, and (iii) the intensity at the absorber surface. Table 1 shows the modeling results of placing a 5-cm diameter aperture and lens at the focus of the primary concentrator. We find that the beam waist decreases with decreasing focal length, but the divergence increases, decreasing both the height and average intensity at the absorber. While using more mirrors increases the intensity, this also increases the waist and decreases the height. The 3-mirror subarray with a 6-cm focal length lens should deliver sufficient intensity while allowing for a cavity with a small aperture for efficient solar absorption.

It is important to note that the small size of the demonstration thermoelectric module requires the optics to focus the beam to a waist that is considerably smaller than the absorber to benefit from the cavity. In scaled-up modules for commercial use, many thermoelectric unicouples would be combined into much larger modules, significantly reducing the constraints on the optics and allowing for larger beam waists while maintaining the high ratio of absorber area to waist area (A_d/A_w) required for an efficient optical cavity.

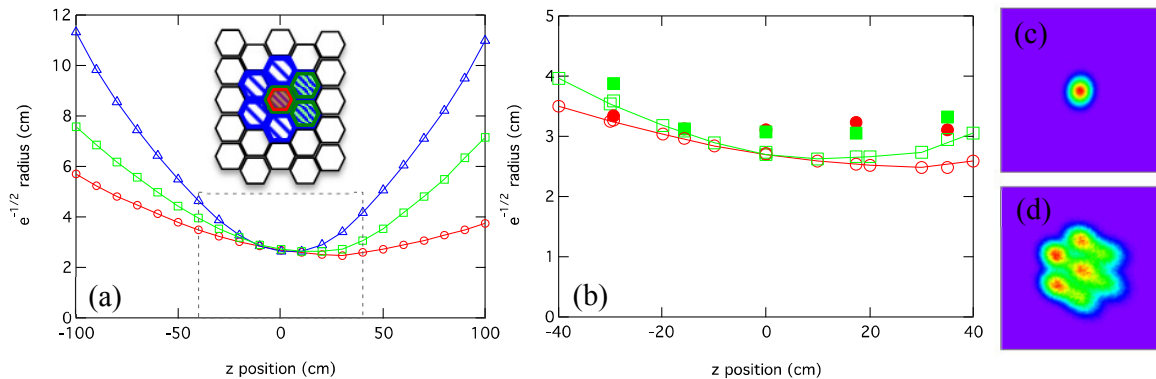


Fig. 4. Geometry of the concentrated beam delivered by the HFSF. (a) Modeled Gaussian beam radius as a function of position for 1 mirror (red circles), 3 mirrors (green squares), and 7 mirrors (blue triangles) of the primary concentrator. The inset shows a schematic of the mirror subsets. (b) Detail of the dashed box in (a) showing agreement between the modeled (open symbols) and experimentally measured (solid symbols) sizes of the concentrated beam in the vicinity of the focus for the 1- and 3-mirror subarrays. False-color modeled intensity profiles for the 7-mirror subarray are shown for $z = 0$ (c) and $z = 80$ cm from the focus (d). Both show a 50 cm x 50 cm area.

Table 1. Modeled secondary optics. The “height” column is the distance from the focus of the lens at which the beam has expanded to completely fill the absorber area ($A_a = 5.3 \text{ cm}^2$). An entry of “–” indicates that the waist area is larger than the absorber area.

Lens focal length (cm)	Number of mirrors	Height (cm)	Average Intensity (Suns)	A_d/A_w
12.5	3	–	800	0.5
12.5	1	5	210	2.6
9	3	2	750	1.3
9	1	4.5	150	4.8
6.25	3	2.5	460	3.2
6.25	1	3.5	140	10.9

4. Assessing the value proposition of terrestrial STEGs

The proposed STEG technology relies on a $T_H = 1000 \text{ }^\circ\text{C}$ that requires the use of concentrating optics. To assess the most promising technical-improvement and cost-reduction pathways for this technology, the NREL team has developed a techno-economic analysis that is based on a detailed understanding of related solar energy technologies—i.e. concentrating solar power (CSP) systems

By leveraging existing optical concentration technology such as that used in CSP systems, the STEG may be configured as either a stand-alone power conversion device or as the topping cycle in a combined STEG-CSP system. Variations of each pathway include both linear- and point-focus systems; however, the theoretical maximum concentration ratios for linear systems (up to 200x), such as trough-based CSP does not appear adequate for the objective hot-side operating temperature and cavity design of the STEG prototype.

4.1. Stand-alone STEG system costs

Tower- and dish-based CSP collector systems may be configured with a STEG device, rather than a traditional CSP power block, and without the accompanying balance of plant (BOP) equipment needed to manage heat transfer fluids. These modifications will, of course also change the operating characteristics of the system—for example, by eliminating much of the thermal inertia associated with power from a CSP system. NREL’s System Advisor Model (SAM) was used to generate a first-order estimate of cost and performance for the integration of a STEG power

converter into tower and dish systems. In these scenarios the capital and operating cost of the current Rankine or Stirling power cycle was eliminated from the SAM model and replaced by a zero-cost STEG device with an efficiency of 5% to 40%. The performance results were used to determine the allowable cost of the STEG device that achieved a levelized cost of electricity (LCOE) equivalent to the current CSP technology. While operating at a higher absorber temperature, no correction was made for lower optical or thermal efficiencies. These assumptions favor the STEG device and therefore provide a “best case” scenario for integration of STEG into a tower or dish collector system.

Results of the first-order analysis are shown in Fig 5. Conventional CSP power blocks have gross conversion efficiencies of 30% to 40%, and this is reflected in the required efficiency that a STEG device would need to achieve to match the performance of the current technology. Relative to conventional CSP energy costs today, the dish-based system architecture appears more promising for stand-alone STEG technologies. Not only is the breakeven point lower – a gross power conversion efficiency of 20% – but dish collectors currently run at temperatures more in line with expected STEG operating temperatures. At a power conversion efficiency of 25%, the STEG budget (additional capital cost at which LCOE is breakeven with CSP) rises to approximately \$500/kWe, assuming we realize the potential benefits in lower O&M costs. A more detailed system-level analysis is required to quantify the potential cost savings associated with a STEG, rather than Stirling-engine-based dish system. For example, a simpler, lighter STEG converter could reduce mechanical requirements and cost of the dish collector.

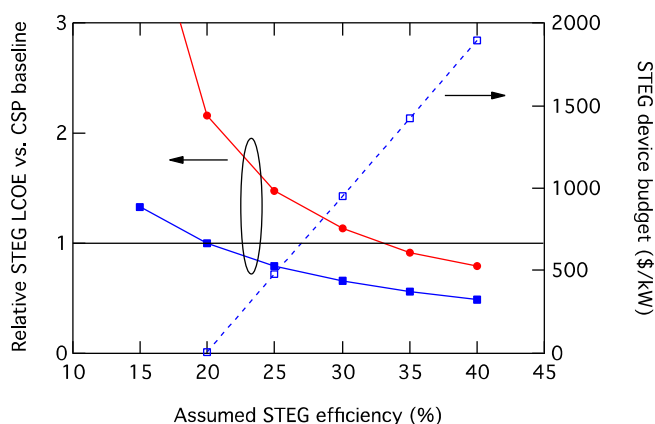


Fig. 5. First-order stand-alone system costs: Assuming the solar irradiance of Daggett, CA, without subsidy, ideal case with STEG CAPEX = \$0, O&M costs cut in half and no change in CSP design to achieve desired operating temperatures. The solid symbols represent the relative LCOE compared to CSP for tower-based (red circles) and dish-based (blue squares) STEG systems, with the break-even point indicated by the horizontal black line, and correspond to the left-hand axis. The open symbols represent the allowed budget for the cost of the STEG device in the dish configuration and correspond to the right-hand axis. As a derivative of conventional point-focus CSP system, the dish-STEG architecture appears most promising.

4.2. Topping cycle STEG system costs

A second, and perhaps more promising, potential commercial pathway for the STEG technology, includes use of the device as a topping cycle for conventional CSP systems. In this scenario, the operating temperatures of the CSP bottom cycle (574 °C) would not change, but the CSP heat transfer fluid would act as the active cooling for the STEG device running at a hot-side operating temperature of approximately 1000°C. Unlike the standalone system scenario considered above, the capital and O&M costs, and operating characteristics of the CSP are not assumed to change with the addition of the STEG topping cycle.

The first-order analysis results are shown in Fig. 6. Here, any electricity generated by the STEG increases the total efficiency of the combined system and results in a decreased LCOE for all non-zero efficiency STEGs. As the gross efficiency of the STEG cycle rises, the available budget for the device also increases. At an efficiency of 25%, the STEG device may cost >\$2500, and the system is expected to break even with conventional CSP. While the

results of Fig. 6 are encouraging, the limiting assumption in this scenario is that the efficiency of the CSP system does not change despite the addition of the STEG. The next step is a more detailed assessment of the system design and efficiency to explore the potential of STEG in this application.

4.3. STEG device manufacturing costs

To assess the commercial viability of STEG devices for use in terrestrial applications, the NREL team will continue to consider (model) the performance and cost implications of the standalone dish-based STEG system, as well as the combined (topping) cycle STEG. The refined system cost analysis will provide a more reliable estimate of the STEG budgets, and the basis for assessing the results of the detailed STEG device manufacturing cost analysis.

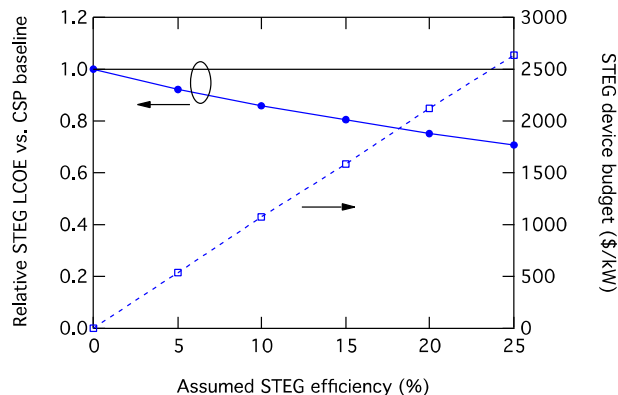


Fig. 6. First-order combined-cycle system costs: Placing a STEG unit as a topping cycle over a conventional CSP power tower could lower overall LCOE. The solid symbols show the calculated reduction in LCOE with the addition of a STEG, while the open symbols show the allowable budget for the STEG. The calculation assumes the solar irradiance of Daggett, CA without subsidy, with no change in the CSP design to achieve the desired operating temperatures.

5. Conclusions

We are undertaking a project with the specific goal of demonstrating a 15%-efficient STEG. Prior demonstrations of STEG technology have achieved limited efficiencies (~5%) due to the low Carnot efficiency from a small temperature drop and the limitations of the ZT for the materials used. Achieving the targeted efficiency requires integrating a high- ZT thermoelectric device with high levels of optical concentration and efficient solar-energy-to-heat conversion to create a large temperature drop across the device. The prototype design includes improved solar-selective absorber materials and a thermally insulating cavity to ensure high absorptivity of solar radiation while minimizing heat losses. The challenge of coupling the required solar concentration to the STEG will be met by tailoring the output of NREL's HFSF. In addition to the experimental demonstration, we are developing a detailed economic model to identify promising pathways to establish STEGs as a viable terrestrial energy-generating technology.

Acknowledgements

Funding for this project is provided by the Advanced Research Projects Agency-Energy, U.S. Department of Energy, Award Number DE-AR0670-4918. NREL's prime contract award number is DE-AC36-08GO28308. The authors also thank A. Lewandowski for providing the HFSF SolTrace input file.

References

- [1] Bell LE, Cooling, heating, generating power, and recovering waste heat with thermoelectric systems. *Science* 2008; 321:1457-1461.
- [2] Yang J, Stabler F, Automotive applications of thermoelectric materials. *J Electron Mater* 2009; 38:1245-1251.
- [3] Caillat T, et al., Progress status of the development of high-efficiency segmented thermoelectric couples. *Nuclear and Emerging Technologies for Space*, 2012.
- [4] Rowe DM, Bhandari CM, *Modern thermoelectrics*. Reston: Reston Publishing Company; 1983.
- [5] Baranowski LL, Snyder GJ, Toberer ES, Concentrated solar thermoelectric generators. *Energy & Environmental Science* 2012;5:9055-9067.
- [6] Telkes M, Solar thermoelectric generators. *J Appl Phys* 1954; 25:765-777.
- [7] Kraemer D, et al., High-performance flat-panel solar thermoelectric generators with high thermal concentration. *Nat Mater* 2011;10:532-538.
- [8] Ma Y, et al., Enhanced thermoelectric figure-of-merit in p-type nanostructured bismuth antimony tellurium alloys made from elemental chunks. *Nano Lett* 2008; 8:2580-2584.
- [9] Yan X, et al., Experimental studies on anisotropic thermoelectric properties and structures of n-type $\text{Bi}_2\text{Te}_{2.7}\text{Se}_{0.3}$. *Nano Lett* 2010;10:3373-3378.
- [10] Snyder GJ, Toberer ES, Complex thermoelectric materials. *Nat Mater* 2008;7:105-114.
- [11] Minnich AK, et al., Bulk nanostructured thermoelectric materials: Current research and future prospects. *Energy & Environmental Science* 2009;2:466-479.
- [12] Vineis CJ, et al., Nanostructured thermoelectrics: Big efficiency gains from small features. *Adv Mater*. 2010;22:3970-3980.
- [13] Bux SK, Fleurial J-P, Kaner RB, Nanostructured materials for thermoelectric applications. *Chem Commun* 2010;46:8311-8324.
- [14] Toberer ES, May AF, Snyder GJ, Zintl chemistry for designing high efficiency thermoelectric materials. *Chem Mater* 2009;22:624-634.
- [15] Kennedy CE, *High-temperature solar selective coating*. 2007.
- [16] Siegel R, Howell JR, *Thermal radiation heat transfer*. New York: Taylor & Francis; 2002.
- [17] Howell JR, *A catalog of radiation heat transfer configuration factors*. University of Texas at Austin; 2010.
- [18] Wendelin T, SolTrace: A new optical modeling tool for concentrating solar optics. *Proceedings of the ISEC 2003: International Solar Energy Conference*, 15-18 March 2003, Kohala Coast, Hawaii 2003;253-260.